ARNICA@TNG: Performance Assessment and Forecast for NICS

L. K. Hunt
C. A. I. S. M. I. - C. N. R.
Largo E. Fermi 5, I-50125 Firenze, Italy
Electronic mail: hunt@arcetri.astro.it

F. Ghinassi
Telescopio Nazionale Galileo
Roque de Los Muchachos Astronomical Observatory
La Palma, Canary Islands, Spain
Electronic mail: ghinassi@tiber.tng.iac.es

R.Maiolino
Osservatorio Astrofisico di Arcetri
Largo E. Fermi 5, I-50125 Firenze, Italy
Electronic mail: maiolino@arcetri.astro.it

ABSTRACT

This report describes the performance of the Arcetri near-infrared camera, ARNICA, mounted at the Telescopio Nazionale Galileo (TNG) during 1999. Since ARNICA's performance has been amply documented at other telescopes, here we emphasize aspects that are relevant to the new infrared camera-spectrometer NICS, such as camera alignment and spatial and derotator variation of the point-spread function and photometry. We also present estimates of the camera+atmosphere efficiency, sensitivity, and telescope emissivity, and compare them with values obtained at other telescopes.

1. Introduction

Almost seven years have passed since the Arcetri near-infrared (NIR) camera, ARNICA, was first mounted at TIRGO in 1992 (Lisi et al. 1993; Lisi et al. 1996; Hunt et al. 1996). During the time that the camera has been in operation, it has acquired more than 60 Gigabytes of data (about half a million frames) and has been mounted at six different telescopes. Here we present recent results from ARNICA mounted at the 3.58-m, f/11 Telescopio Nazionale Galileo (TNG)[1] during 1999. A performance assessment of ARNICA mounted at three other telescopes from 1995 to 1997 is given in Hunt & Mannucci (1998), and the initial campaigns (1992-1994) at TIRGO and the William Herschel Telescope (WHT) are documented in Hunt et al. 1996, and a series of technical reports (Hunt et al. 1994a, 1994b, 1994c). The camera, ARNICA, relies on a NICMOS3 256×256 1–2.5 μm HgCdTe scientific grade array, and at TNG provides a 90×90 arcsec^2 field-of-view (FOV), with a scale of 0.35 arcsec pixels (after June, 1999; 0.40 arcsec pixels before).

Because the new near-infrared camera NICS, based on a HgCdTe 1024×1024 array, is due to arrive at the TNG in November, 1999, the time is ripe for assessing issues germane to the new camera. In this report, we have therefore analyzed alignment characteristics and variation of the point-spread function (PSF) and photometric response with derotator angle and position on the detector. We also estimate system efficiency, sensitivity, emissivity and compare them to values obtained with ARNICA mounted at other telescopes.

2. Observations and image reduction

We have analyzed ARNICA data primarily from three photometric nights (3–5 August 1999) which were allocated specifically for this purpose. During this dedicated period, we concentrated on the acquisition of data relevant to evaluating alignment effects and optical quality, but also performed several photometry tests, and gathered emissivity data. We have also used data from other nights, acquired in an earlier run (February), to derive sensitivity and efficiency in the various filters. Photometric calibration was performed by observing stars from the list of Hunt et al. (1998).

Data reduction was standard using ordinary sky flats in J and H, and differential sky flats in K and K_s (see Hunt et al. 1996). Briefly, "ordinary sky flats" are those derived from some subset (usually close in time and space to the observation of interest) of the sky frames during the night. With this reduction, a sky frame is not usually subtracted, but rather normalized and divided, and then a constant sky level can be subtracted. Alternatively, "differential sky flats" must be acquired at the beginning or the end of the night in order to obtain the mean of several frames with a count level substantially higher than normally observed during the night ("ON"). The mean of several low-level frames acquired with the same integration time and coadds ("OFF") is subtracted from the ON average, then normalized to the median difference count level. The resultant frame (differential flat) is used to flatfield frames where there is an additive contribution to the background, such as in K where the telescope produces a spatially-varying emissive

[1] TNG is operated by the Consorzio Nazionale per l'Astronomica e l'Astrofisica, Roma.

component. In this reduction, a local (in space and time) frame or mean of frames is *subtracted* as sky, and the difference is *divided* by the differential flat. As in the optical, differential flats can also be acquired by observing the dome, but the quality of dome flats depends on the uniformity of illumination.

3. Alignment effects

To assess the quality of the optical alignment (ARNICA–derotator axis, ARNICA–telescope optical axis), we acquired a set of standard star observations obtained by keeping the telescope fixed, and rotating the derotator. To visualize the pupil image of the optical configuation as well as possible, we repeated the measurement but defocused the star. We also acquired two sets in each filter (J, H, K, and Kc) of a bright standard star placed in a grid of 8×8 positions on the array, with a separation of roughly 11 arcsec between each measurement. The grid measurements are discussed in the next two sections (3.1 and 3.2), and those with the derotator in Section 3.3.

3.1. Spatial variation of photometry

The standard deviation σ of the photometry over the entire 8×8 grids (64 measurements) is 0.050 mag in J, 0.042 in H, 0.056 in K, and 0.048 in K_s. (These last three are the means of the σ in two independent grid repetitions.) These spreads are similar to the nightly σ of the photometry in a single position, except for J where the nightly spread is roughly 30% smaller.

The spatial variation of the photometric zero points (ZPs) in the 8×8 grids is shown schematically in Figure 1. All grids were obtained with the same telescope pointing sequence, which foresees a return to the starting point after every two columns. The rather irregular pattern evident in the figure is due to telescope "wandering" for a few of the grids. The ZPs are the magnitude that corresponds to a signal of 1 ADU/second, and the larger they are, the more efficient the system is. The vertical dotted lines correspond to the mean ZP of the entire grid, and the vertical dashed lines to the residual relative to the mean. Both vertical lines are positioned horizontally at the mean in x of the columns of the grid; thus the horizontal excursions are photometric, not positional. The deviations to the right of the vertical dotted lines (mean ZP along the column) correspond to ZP excesses (more counts than the mean), and ZP deficiencies (fewer counts than the mean) fall to the left. The amplitude of these excursions can be measured with the horizontal solid line in the lower right corner of the figures, as it corresponds to 0.1 mag excursion.

The H, K, and K_s grids show very little systematic deviations along the columns, while the J band, as suggested also by the relatively high σ_J, shows the largest systematic spatial variations of all the filters. The J band thus shows evidence for an extra component to the background, not properly accounted for in the data reduction.

3.1.1. Additive component in J

Already in the February data, there was some doubt raised about the possibility of stray light in J because of spatial variation of the photometry. Consequently, in the August run, we acquired differential sky flats also in J and H so that the two different flatfields could be tested. We have used these differential flats to re-reduce the J- and H-band data, and the resulting photometry from the 8×8 grids is shown in

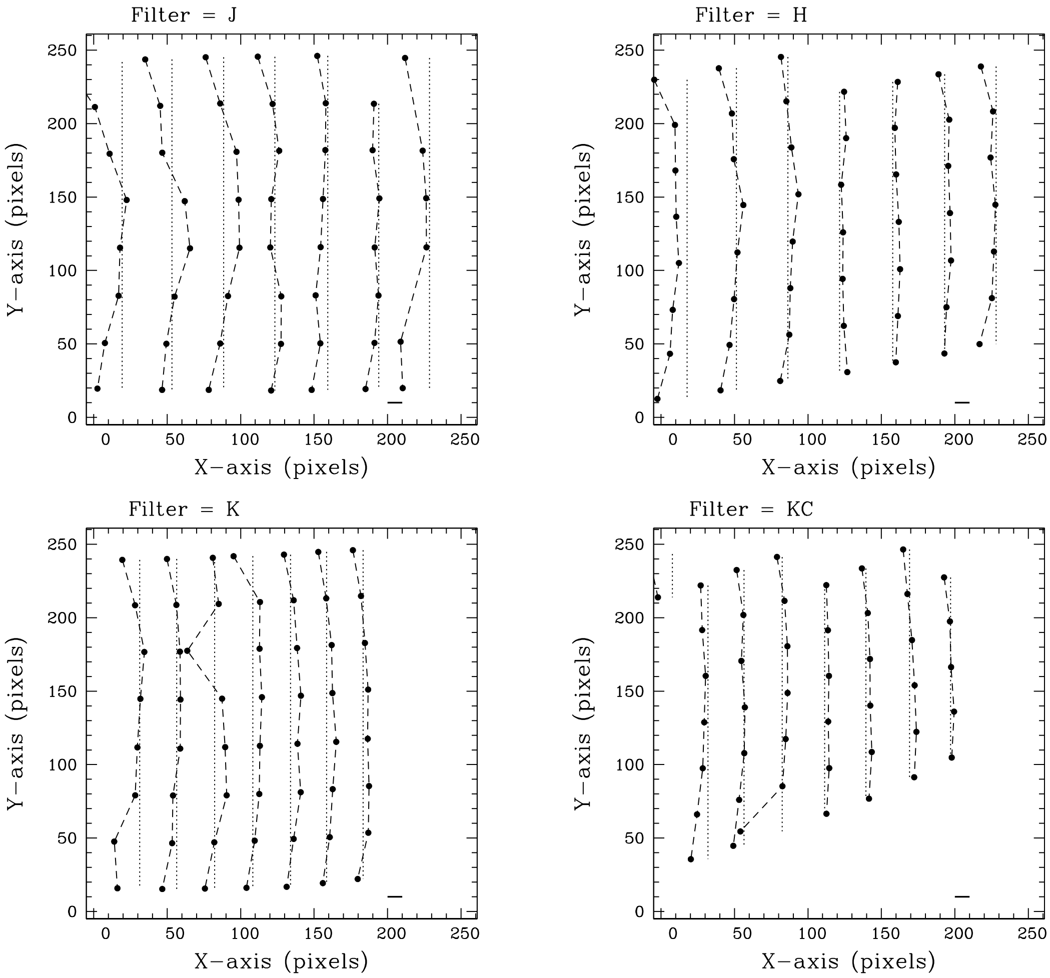

Fig. 1.— Variation of the photometric ZP as a function of position. The J band is shown in the top left panel, the H in the top right, K in the bottom left panel, and K_s in the bottom right. The small horizontal line in the lower right-hand corner corresponds to 0.1 mag deviation. The vertical dotted lines correspond to the mean ZP of the entire grid, and the vertical dashed lines to the residual relative to the mean. Both vertical lines are positioned horizontally at the mean in x of the columns of the grid; thus the horizontal excursions are photometric, not positional. Note that here the J and H bands were flat-fielded with flats derived from the night sky, and K and K_s with differential sky flats. The discrepant point in the third column of the K panel is due to a bad pixel.

Fig. 2. While the difference between the two reductions is undetectable in H, in J, it is clearly evident. The standard deviations over the 64-star grids confirm the impression: the spread in J with differential flats is 0.034 mags, a reduction of more than 30% relative to the ordinary flat reduction. In H, σ increases from 0.042 to 0.045 mag, so that there is no improvement with differential flats.

Reduction with differential flats in principle remove a stable additive component. Therefore, this extra component in J must be stable in time and space, and, since it is *not* detectable in H, we surmise that it is light-related, rather than due to other origins such as blackbody emission as seen in K and K_s. The extra J-band component of the background is probably stray light, although obvious sources susch as lights left on in the dome or at the Nasmyth are excluded. Its origin is under investigation.

3.2. Spatial variation of the PSF

The results of fitting an elliptical gaussian to the stellar images in the 8×8 grids is shown in Fig. 3. We have combined without distinction the grids acquired in the different filter bands, which results in a total of 476 data points.

It is evident from Fig. 3 that the largest, most elliptical PSFs appear in the lower-right quadrant, an effect that was present also in February. The smallest, most circular PSFs appear in the left half of the array, and perhaps preferentially in the upper-left quadrant. Moreover, in the lower-right quadrant, the long axis of the ellipse fit *always* points left and upwards. Nevertheless, the data are sufficiently noisy that it is not straightforward to deduce alignment characteristics from them.

To formulate a better idea of the spatial variation of the PSF, we derived average axial ratios and geometric means of the semi-major and semi-minor axes in the ellipse fittings. These average values were calculated by dividing the array into a 3×3 grid. The values of the mean axial ratios for each of the nine boxes are shown in the left panel of Fig. 4, and the mean geometric means in the right panel. In both figures, the symbol size is related to 20 times the difference from unity. Figure 4 shows perhaps more clearly than Fig. 3 the effect of misalignment of the optical axis of the camera. The left panel illustrates the mean axial ratios σ_x/σ_y, and the trend of larger ratios from left to right is evident. The right panel is clearer still. If we consider only the mean size of the PSF, that is to say $\sqrt{\sigma_x\,\sigma_y}$, independently of its orientation, Fig. 4 shows that the largest spots occur in the lower-right corner, and the smallest in the lower-left corner.

3.3. PSF and "pupil image" variation with derotator position

Here we discuss the measurements obtained with the telescope fixed in one position, but rotating the derotator between frames. The derotator fiducial position that gives the α, δ directions along the rows and columns of the array is 26°. The top panel of Fig. 5 shows the superposition of five defocused images, acquired on 4 Aug 99; the bottom panel shows the superposition of three focused images acquired on 5 Aug 99. In both cases, the number of images corresponds to the number of derotator positions.

Both sets of images (focused and defocused) can be used to determine the mechanical center of the derotator. Using a geometrical method, we determine the center of the defocused superposition image to be $(x_c, y_c) = (52.3\pm4.0,\ 160.4\pm1.4)$ pixels. The same method applied to the focused superposition images gives the center as (64.1,153.1). Between the two nights the derotator axis changed by roughly 10 pixels in x and y, a change that could result from flexure in the telescope structure, or a different set of pointing

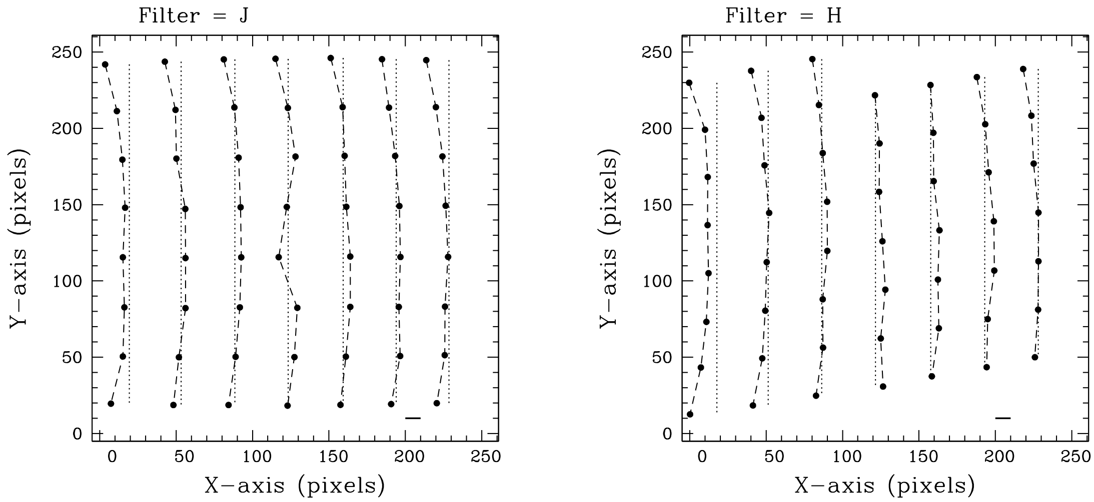

Fig. 2.— Variation of the photometric ZP as a function of position, but using differential skyflats as the flatfield. (Fig. 1 shows the results obtained with K and K_s differential flats.) The left panel shows J, and the right panel shows H. As before, the small horizontal line in the lower right-hand corner corresponds to 0.1 mag deviation; the vertical dotted lines correspond to the mean ZP of the entire grid; and the vertical dashed lines to the residual along the column relative to the mean. Both vertical lines are positioned horizontally at the mean in x of the grid columns; thus the horizontal excursions are photometric, not positional.

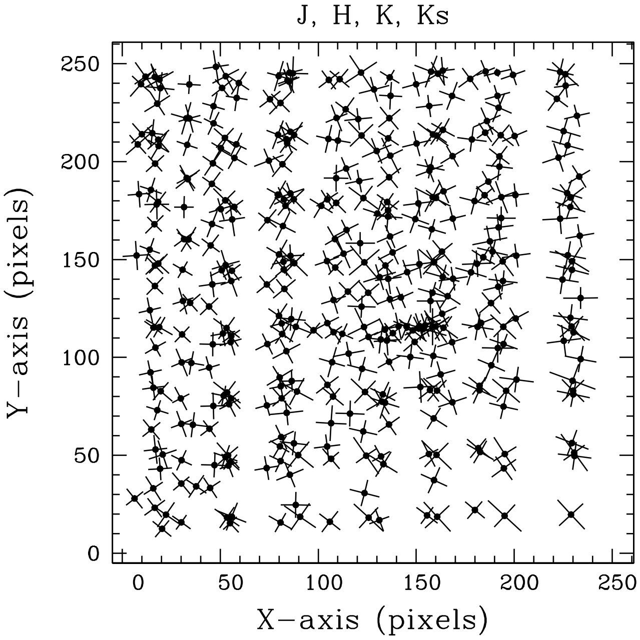

Fig. 3.— Elliptical gaussian fits of all the PSFs acquired in the 8×8 grids. All filters are combined which gives a total of 476 data points and PSF fits.

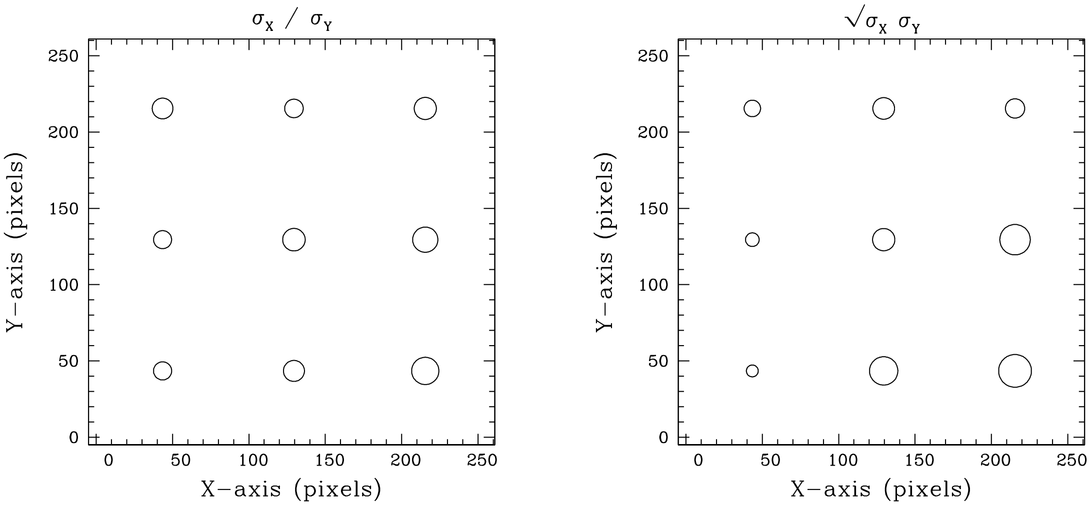

Fig. 4.— Parameters of the elliptical gaussian fits averaged over a 3×3 grid. Mean axial ratios of the ellipse axes are shown in the left panel; geometric means in the right. In both figures, the symbol size is related to 20 times the difference from unity.

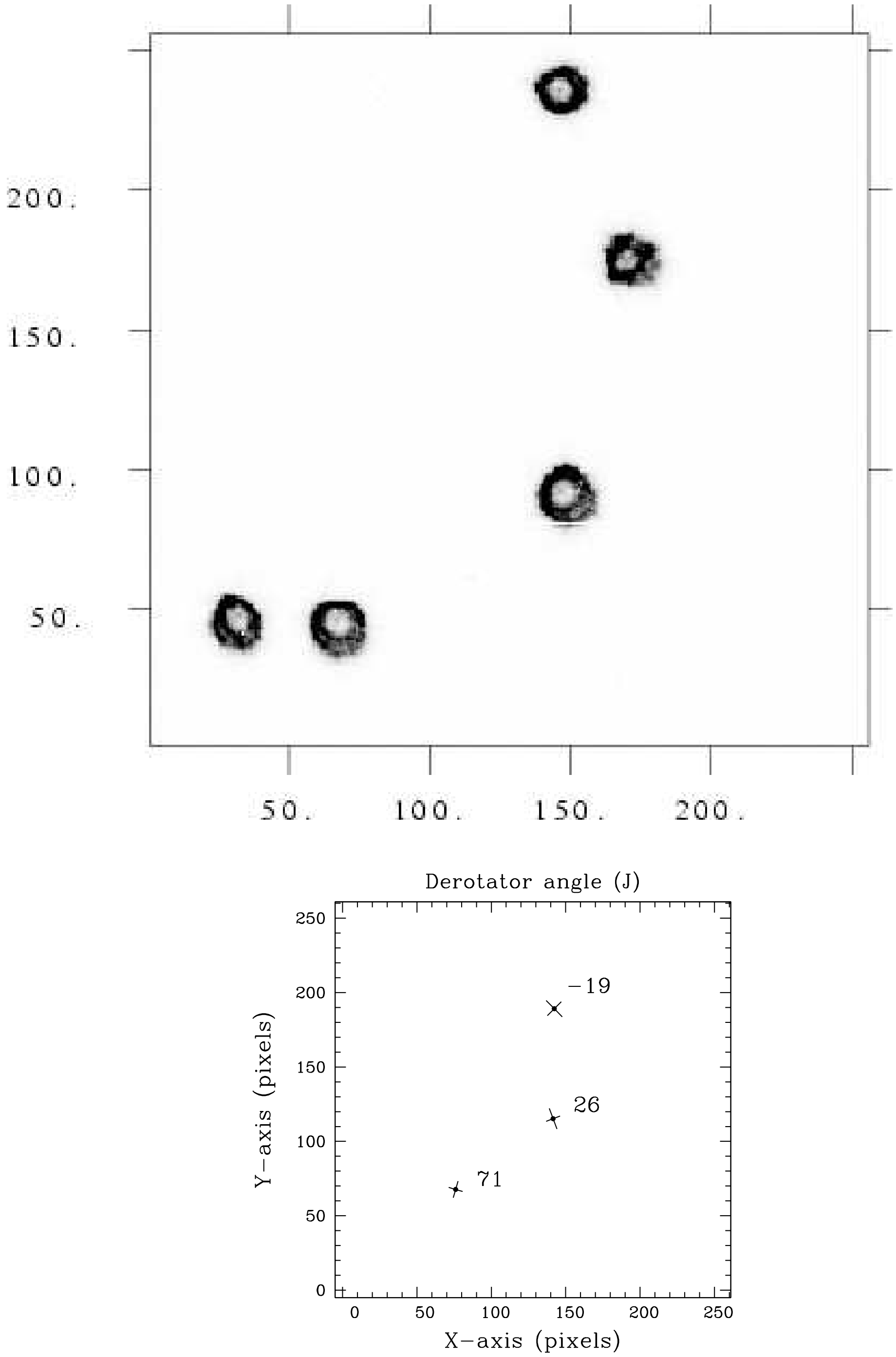

Fig. 5.— Variation of the PSF as a function of derotator angle (with telescope fixed). The defocused image is shown in the top panel, and the focused one (schematically) in the bottom panel. The top panel is the composition of five measurements, taken at different derotator initial angles as follows (from top clockwise): −50°, −19, +26, +71, and +85. The bottom panel (also a composition) illustrates the PSF fits to elliptical gaussians, as described in the text, and also as shown in Fig. 3. The derotator angles (in degrees) are labelled.

parameters. As a matter of fact, between the two nights, the pointing algorithm was changed. The center of rotation of the derotator is offset from ARNICA's detector center by roughly 27 arcsec in the horizontal direction, and 11 arcsec in the vertical direction (of the array).

We can also use the asymmetry of the defocussed stellar images to estimate the position of ARNICA's optical axis. The top panel of Fig. 5 shows clearly that the defocused images are asymmetric, and apparently comatic; the obscuration of the secondary is clearly visible, and displaced (in the worst cases towards the bottom of the figure) from the center of symmetry of the surrounding ring. The direction of the widest part of the image "doughnuts" points away from the optical axis, so that we can derive its position from them. The ellipse fits of the focused PSF shown in Fig. 3 are consistent with this geometry, as comatic images, when fit by an ellipse, are elongated with the long axis pointing towards the optical axis (see Section 3.2). Using the asymmetry of the defocused images, and determining the centers of the doughnuts visually, we estimate the position of ARNICA's optical axis to be roughly (54,213). This position is 74 and 85 pixels, respectively, from the detector center, and some distance above the derotator axis.

This displacement of the optical axis of the camera from the center of its detector causes an aberration of the PSF that is worst in the lower right quadrant. Such an effect explains the clearly comatic defocused images in Fig. 5, but also the results of Section 3.2 where we found that the worst image quality was obtained in the lower right corner of the array. The corrected FOV of the f/11 optics used for ARNICA@TNG is roughly 128 pixels in radius, which implies that even in the best case (of the optical axis coincident with the detector center), the vertices of the array (at pixel radii of $128\sqrt{2}$) will present aberrations. For the displacement implied by our measurements, notable aberration in the PSF occurs at roughly $x \geq 180$, and $y \leq 85$ pixels.

The aberration observed in our images is worse than it would be ordinarily, because the optical train of the camera was installed incorrectly during the servicing at the Infrared Laboratories (Tucson, Arizona) in May, 1999. After that operation, the pixel scale changed by 10% (from 0.397 to 0.352 arcsec/pixel), and the optics are in a configuration that is not the designed one. This topic is discussed in more detail in the next section.

4. Astrometry and the transformation from pixels to equatorial coordinates

We have derived a "plate solution" from stellar fields observed for calibration, and find for the August data that the pixel scale is 0.352 arcsec/pixel (and the same in x and y to within 0.001 arcsec/pixel). The orientation of the array rows and columns with the cardinal directions (α and δ) is good to within 0.25 and 0.2°, respectively, with the 26° derotator fiducial angle noted previously. The orientation of the images (as seen with saoimage) is North down, and East to the right, that is to say inverted relative to the canonical Sky Survey orientation of North up and East to the left. The pixel scale is roughly 10% smaller than before the repair at Infrared Laboratories (see above), and before the intervention corresponded to the theoretical expectation of the f/11 optical train (0.40 arcsec/pixel).

5. Efficiency, sensitivity, and seeing in J, H, K, and Ks

Sensitivity calculations, flux conversions, and filter characteristics are as given in Hunt et al. (1994b). The only exception is that here point-source limiting magnitudes for a given night are derived using an effective aperture whose diameter is defined by twice the FWHM of the median point-spread function (PSF) measured on that night. In all sensitivity estimates, the collecting area is given by the difference of the primary and secondary mirror diameters. Table 1 reports the results our analysis for the different runs (February and August). The various columns (sky, FWHM) report complete nightly medians that typically involve hundreds of frames. The efficiency η is a global value, and takes into account losses from the atmosphere, the telescope, and the camera.

The efficiency of ARNICA@TNG is higher than at most of the other telescopes that the camera has been hosted by, comparable only to ARNICA@VATT (Hunt & Mannucci 1998). The TNG is one of the two most efficient telescopes, being roughly 0.05 better in J and 0.1 better in H and K than the WHT (measured in 1993, see Hunt et al. 1996).

In a background-limited regime, sensitivities scale with the square root of the background and the linear size of the aperture. The seeing at TNG is typically good at 1.0 arcsec or better in all four bands, and occasionally the seeing can be very good. Two of the three nights in the August run were characterized by sub-arcsec mean FWHMs.

Because of its consequence on sensitivity, we have also examined the backgrounds observed at TNG in the different filters. The mean J background was the same to within 0.1 mag in February and August, while the K_s background was a factor of three greater in August than previously. (H and K data are not available in February.) The observed K background during August is also much brighter than that measured during other La Palma runs at other telescopes: 10.6 mag/arcsec^2 at TNG, 11.8 at WHT (December), 11.6–1.7 at NOT (Hunt et al. 1996; Hunt & Mannucci 1998). The NOT values were measured in August-September, although ambient tempuratures were higher during the TNG run (14° C) than in the previous NOT runs (7–8° C). Because of the higher K_s background, point-source sensitivities in K_s are lower by roughly 0.5 mag in August than in February.

The sensitivity of ARNICA@TNG is comparable to that obtained at WHT, a convenient comparison since it is another 4-meter class telescope at the same site. In particular, the (3σ, 60 sec) point-source magnitude limits are similar in J (20.7 at WHT, 20.6 at TNG) and H (19.7 WHT, 19.9 TNG), even though WHT is larger than TNG by 62 cm. However, the point-source sensitivity in K (and K_s) is compromised by the high background: we obtained 18.8 mag in K at WHT, but only 17.9 at TNG. In February, in K_s, with the lower background, the limiting point-source magnitude was 18.6, but in August it was 18.1, 0.5 mag lower.

6. Background and telescope emissivity

The measurement of telescope+instrument emissivity is given by the ratio of two quantities: 1) the non-atmospheric contribution to the measured background (NAB), and 2) the flux density from a blackbody. Typically, for the blackbody measurement (BB), one observes an unlit dome or the closed mirror covers. The NAB can be derived from a regression of sky versus airmass, if we assume that the true sky background is proportional to atmospheric path length. Alternatively, if we have measurements at airmasses (am) 1 and 2, then the NAB can be derived with the simpler expression, NAB=[am1 - (am2-am1)]. In both cases, emissivity is therefore NAB/BB.

We have used this last expression to derive the emissivity, using as a blackbody the cooled mirror covers. The K-band emissivity so derived, measured in August 1999, is roughly 68%. Such a high value

Table 1. ARNICA@TNG: efficiencies, sensitivities, backgrounds, and PSF's

	η Sky (mag arcsec^{-2}) FWHM (arcsec)				Extended Source (mag arcsec^{-2})[a]				Point Source (mag)[b]			
Date	J	H	K	K_s	J	H	K	K_s	J	H	K	K_s
99feb10	–	–	–	0.50	–	–	–	18.3	–	–	–	18.6
	–	–	–	12.4								
	–	–	–	1.13								
99feb19	0.30	–	–	0.53	20.3	–	–	18.4	20.7	–	–	18.6
	15.6	–	–	12.6								
	0.98	–	–	1.21								
99mar02	–	–	–	0.53	–	–	–	18.3	–	–	–	18.6
	–	–	–	12.4								
	–	–	–	1.09								
MEAN	0.30	–	–	0.52	20.3	–	–	18.3	20.7	–	–	18.6
	15.6	–	–	12.5								
	0.98	–	–	1.14								
99aug03	0.23	0.45	0.43	0.45	20.1	19.2	17.3	17.6	20.8	19.9	18.0	18.3
	15.6	13.8	10.7	11.3								
	0.83	0.80	0.80	0.83								
99aug04	0.22	–	0.42	0.43	20.2	–	17.3	17.5	20.7	–	17.8	18.0
	15.9	–	10.6	11.2								
	0.99	–	0.94	1.03								
99aug05	0.21	0.43	0.41	0.43	20.0	19.4	17.2	17.5	20.4	19.9	17.7	18.0
	15.6	14.3	10.6	11.2								
	1.11	0.95	1.03	1.03								
MEAN	0.22	0.44	0.42	0.44	20.1	19.3	17.3	17.5	20.6	19.9	17.9	18.1
	15.7	14.0	10.6	11.2								
	0.98	0.87	0.92	0.96								

[a] Calculated at 3 σ, in 60 sec.

[b] As a, and assuming a virtual aperture of twice the FWHM (third row, Cols. 2–5).

can be partially attributed to the temperature reduction of the actively cooled mirror covers, and the consequent lack of thermal equilibrium with the environment. When this measurement was repeated using ambient-temperature mirror covers, the measured K-band emissivity was 46%. Part of this still high value may be due to the abnormally high background levels, although another contributor may be the folding mirror M4 in ARNICA's optical path at the Nasmyth focus.

7. Concluding remarks

The three main problems with ARNICA@TNG are its optical misalignment, the stray light in J, and the high background in K and K_s. Part of the high background may be caused by the heat of the summer, since the K_s background was a factor of three lower in February than in August. A detailed monitoring of the sky background as a function of lunar phase and ambient temperature is needed. In any case, investigations are underway to better understand the cause of all these problems. In spite of them, TNG with ARNICA is as sensitive in J and H (and K_s in February) than WHT, with a diameter 62 cm smaller.

In the seven or so years that ARNICA has been in operation, it has proved to be a rugged "workhorse", able to function efficiently in very different observing situations. This was made possible by ARNICA's modular design; by S. Gennari and F. Lisi who designed and implemented the various optical modules to match the different telescopes (Gennari 1997); and by C. Baffa, V. Gavryusev, and E. Giani who adapted ARNICA's data acquisition software to different telescopes and operating environments. For this report, we are especially grateful to S. Esposito and S. Gennari for enlightening discussions and numerical simulations regarding ARNICA's optics. We hope that the future years will be as fruitful with NICS as these past years have been with ARNICA.

REFERENCES

Gennari, S. 1997, Arcetri Observatory Technical Report N. 2/97

Hunt, L., Maiolino, R., & Moriondo, G., 1994a, Arcetri Observatory Technical Report N. 2/94 (Report I)

Hunt, L.K., Maiolino, R., Moriondo, G. & Testi, L. 1994b, Arcetri Technical Report, N. 3/1994 (Report II)

Hunt, L.K., Testi, L., Borelli, S., Maiolino, R., & Moriondo, G. 1994b, Arcetri Technical Report, N. 4/1994 (Report III)

Hunt, L.K., Lisi, F., Testi, L., Baffa, C., Borelli, S., Maiolino, R., Moriondo, G., & Stanga, R.M. 1996, A&ASS, 115, 181

Hunt, L.K., Mannucci, F., Testi, L., Migliorini, S., Stanga, R.M., Baffa, C., Lisi, F., & Vanzi, L. 1998, AJ, 115, 2594

Hunt, L.K., & Mannucci, F. 1998, Arcetri Technical Report, N. 2/98

Lisi, F., Baffa, C., & Hunt, L. 1993, "ARNICA: the Arcetri Observatory NICMOS-3 imaging camera", Proceedings of SPIE Technical Conference 1946, Orlando

Lisi, F., Baffa, C., Biliotti, V., Bonaccini, D., Del Vecchio, C., Gennari, S., Hunt, L., Marcucci, G., & Stanga, R.M. 1996, PASP, 108, 364

This preprint was prepared with the AAS LaTeX macros v4.0.